Journal of Magnetic Resonance 299 (2019) 12–20

Contents lists available at ScienceDirect

Journal of Magnetic Resonance

journal homepage: www.elsevier.com/locate/jmr

Spin dephasing around randomly distributed vessels

L.R. Buschle [a,b,c], F.T. Kurz [a,b], T. Kampf [d,e], H.P. Schlemmer [a], C.H. Ziener [a,b,*]

[a] German Cancer Research Center – DKFZ, Im Neuenheimer Feld 280, 69120 Heidelberg, Germany
[b] Heidelberg University Hospital, Im Neuenheimer Feld 400, 69120 Heidelberg, Germany
[c] Heidelberg University, Faculty of Physics and Astronomy, Im Neuenheimer Feld 227, 69120 Heidelberg, Germany
[d] University of Würzburg, Department of Experimental Physics 5, Am Hubland, 97074 Würzburg, Germany
[e] Würzburg University Hospital, Department of Neuroradiology, Josef-Schneider-Straße 11, 97080 Würzburg, Germany

ARTICLE INFO

Article history:
Received 13 July 2018
Revised 27 November 2018
Accepted 28 November 2018
Available online 30 November 2018

Keywords:
Spin dephasing
Gradient echo
Relaxation rate
Bloch-Torrey equation
Vessel imaging

ABSTRACT

We analyze the gradient echo signal in the presence of blood vessel networks. Both, diffusion and susceptibility effects are analytically emphasized within the Bloch-Torrey equation. Solving this equation, we present the first exact description of the local magnetization around a single vessel. This allows us to deduce the gradient echo signal of parallel vessels randomly distributed in a plane, which is valid for arbitrary mean vessel diameters in the range of physiological relevant blood volume fractions. Thus, the results are potentially relevant for gradient echo measurements of blood vessel networks with arbitrary vessel size.

1. Introduction

The signal in magnetic resonance imaging depends on tissue properties as well as sequence configurations. By varying sequence parameters as *e.g.* the echo time, different tissue properties such as intrinsic relaxation times T_1 and T_2, magnetic susceptibility distributions, diffusion coefficients, etc. can be measured. In MRI, usually monoexponential relaxation times T_1, T_2 and T_2^* are measured. Hereby, especially the gradient echo relaxation time T_2^* is sensitive to microstructural changes of the tissue [1]. Thus, gradient echo sequences are used in functional MRI [2] or susceptibility weighted imaging [3] to analyze blood oxygenation and susceptibility variations, respectively. Moreover, T_2^*-mapping is used to quantitatively measure the oxygen extraction fraction in cerebral vessel networks [4–6]. In such networks, a susceptibility difference between blood filled vessels and the surrounding tissue exists. Thus, local magnetic field inhomogeneities occur and the signal dephases quickly. However, for small capillaries, diffusion effects of spin-bearing water molecules cannot be neglected since they experience an averaged Larmor frequency. The signal decay therefore slows down. Thus, the gradient echo relaxation time T_2^* depends on the mean vessel size. This effect has been observed more than twenty years ago [7,8] and is used in several applications like vessel size imaging [9,10] or vessel architectural imaging [11]. However, most application either use the relaxation time T_2^* of uniformly distributed vessels in the static dephasing [12] or the motional narrowing limit [13], where diffusion effects can be ignored or predominate, respectively. Recent numerical studies found that the MR signal of non-uniformly distributed vessel arrangements significantly deviates from the MR signal decay of uniformly distributed vessels [14,15], while an analytical expression for arbitrary diffusion strength in blood vessel networks was so far only provided for an infinite domain model [16] or in Krogh's capillary model [17,18].

In this work, we provide a solution for the gradient echo signal around parallel vessels uniformly distributed in a plane that is valid for arbitrary vessel diameters in the range of physiological relevant blood volume fractions and, thus, is highly relevant for vessel radius mapping as well as vessel architectural imaging.

2. General theory

We assume $K \gg 1$ randomly arranged, parallel vessels in a large voxel. Due to the susceptibility difference $\Delta\chi$ between blood and surrounding tissue, local inhomogeneities in the Larmor frequency $\omega(\mathbf{r})$ occur around each vessel of the form:

$$\omega(\mathbf{r}) = \sum_{i=1}^{K} \omega_l(\mathbf{r} - \mathbf{r}_i) \qquad (1)$$

---

* Corresponding author at: German Cancer Research Center, Im Neuenheimer Feld 280, 69120 Heidelberg, Germany.

E-mail address: c.ziener@dkfz-heidelberg.de (C.H. Ziener).

https://doi.org/10.1016/j.jmr.2018.11.014

$$\omega_l(\mathbf{r}) = \delta\omega R^2 \frac{\cos(2\phi)}{r^2}, \tag{2}$$

where $\delta\omega = \gamma B_0 \Delta\chi \sin^2(\theta)/2$ is the characteristic frequency of the dipole field that depends on the gyromagnetic ratio $\gamma \approx 2.675 \times 10^8$ rad s^{-1} T^{-1} and the angle θ between vessel direction and main magnetic field B_0. The vessel radius is denoted as R and the positions of the vessels are denoted as $\mathbf{r}_i$. The position vector is measured in polar coordinates $\mathbf{r} = (r, \phi)$, *e.g.* the distance of the position vector in the cross-sectional plane of the vessel is denoted as r and the polar angle in the cross-sectional plane of the vessel is denoted as ϕ, see Fig. 1 in [19].

The transverse Cartesian components of the local magnetization are summarized to the complex-valued local magnetization $m(\mathbf{r},t) = m_x(\mathbf{r},t) + \mathrm{i}m_y(\mathbf{r},t)$. The local magnetization then is determined by the Bloch-Torrey equation [20] that accounts for diffusion and susceptibility effects:

$$\frac{\partial}{\partial t} m(\mathbf{r},t) = [D\Delta - \mathrm{i}\omega(\mathbf{r})]m(\mathbf{r},t), \tag{3}$$

where $\Delta = \partial_r^2 + r^{-1}\partial_r + r^{-2}\partial_\phi^2$ denotes the two-dimensional Laplace operator and D is the diffusion coefficient. At the initial time point $t = 0$, the local magnetization takes the constant values $m(r,\phi,0) = m_0$. In general, the initial local magnetization m_0 is complex-valued which corresponds to a global phase of the initial magnetization. The vessels are impermeable and, thus, due to the diffusion part of the Bloch-Torrey equation (3), the local magnetization obeys Neumann boundaries at the surface of the cylinders:

$$\frac{\partial}{\partial r} m(r,\phi,t)\Big|_{r=R} = 0. \tag{4}$$

An analytical treatment of the Bloch-Torrey equation (3) seems to be cumbersome, since the Larmor frequency is given as a superposition of the magnetic field inhomogeneities from each vessel. However, Yablonskiy and Haacke showed in the static dephasing regime, where diffusion effects are neglected, that the signal $M(t)$ can be deduced by analyzing the local magnetization $m(\mathbf{r},t)$ around a single cylinder ($K = 1$) [12]:

$$M(t) = M_0 \mathrm{e}^{-\eta f(t)} \tag{5}$$

$$f(t) = \frac{1}{\pi R^2} \int_{r>R} \mathrm{d}^2\mathbf{r} \left[1 - \frac{m(\mathbf{r},t)}{m_0}\right], \tag{6}$$

where $M(t=0) = M_0$ is the initial magnetization and η denotes the regional blood volume fraction, *i.e.* the ratio of blood volume to total volume of the examined tissue. Throughout this work, a small blood volume fraction $\eta \ll 1$ is assumed, which is physiologically motivated [21]. Kiselev and Posse stated that Eq. (6) is in good approximation also valid for non-vanishing diffusion effects [22,23]. In their work, the local magnetization yielded from the slow diffusion approximation that is only valid for large vessel diameter.

3. Exact solution

We extend the relaxation function $f(t)$ in the form

$$f(t) = \frac{1}{\pi R^2} \int_R^\infty \mathrm{d}r r \int_0^{2\pi} \mathrm{d}\phi \left[1 - \frac{m(\mathbf{r},t)}{m_0} - \frac{\partial}{\partial t} \frac{m(\mathbf{r},t)}{m_0}\Big|_{t=0} t\right], \tag{7}$$

and claim that this expression is valid in all diffusion regimes since the added term is zero but guarantees that the integral converges. Details about the derivation and the validity of Eq. (7) are presented in Appendix A. Moreover, we analytically solve the Bloch-Torrey equation to obtain an exact solution of the local magnetization around a single vessel that is valid for arbitrary vessel diameters, see Fig. 1. We now focus on the dephasing around a single vessel.

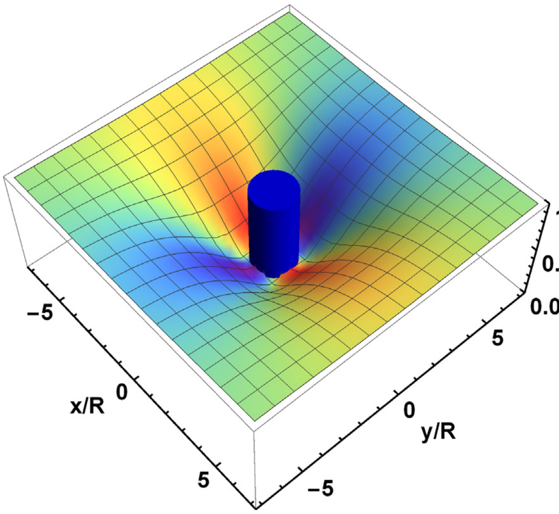

Fig. 1. Local magnetization $m(\mathbf{r},t)$ around a single vessel according to Eq. (15) for $\tau\delta\omega = 4$ and $\delta\omega t = 20$. The z-axis shows the amplitude $|m(\mathbf{r},t)|$, whereas the colors indicate the phase of the local magnetization (red: $\arg(m(\mathbf{r},t)) = +\pi/2$, blue: $\arg(m(\mathbf{r},t)) = -\pi/2$). (For interpretation of the references to color in this figure legend, the reader is referred to the web version of this article.)

To analyze the interplay between diffusion and susceptibility effects, it is convenient to define a diffusion time τ that describes the diffusion strength:

$$\tau = \frac{R^2}{D}. \tag{8}$$

The local magnetization $m(r,\phi,t)$ around a single vessel for arbitrary diffusion strengths is governed by the Bloch-Torrey equation (3) and can be obtained by an expansion ansatz:

$$m(r,\phi,t) = m_0 \sum_{\mu=0}^{\infty} \mathrm{ce}_{2\mu}\left(\phi, \frac{\mathrm{i}}{2}\tau\delta\omega\right) g_\mu(r,t). \tag{9}$$

The Mathieu functions $\mathrm{ce}_{2\mu}(\phi, \mathrm{i}\tau\delta\omega/2)$ for purely imaginary indices are in detail analyzed in [24]. According to the Bloch-Torrey equation (3), the radial eigenfunctions $g_\mu(r,t)$ have to fulfill the equation:

$$\frac{1}{D}\frac{\partial}{\partial t} g_\mu(r,t) = \frac{\partial^2}{\partial r^2} g_\mu(r,t) + \frac{1}{r}\frac{\partial}{\partial r} g_\mu(r,t) - \frac{k_\mu^2}{r^2} g_\mu(r,t), \tag{10}$$

where k_μ^2 are angular eigenvalues:

$$k_\mu^2 = a_{2\mu}\left(\frac{\mathrm{i}}{2}\tau\delta\omega\right) \tag{11}$$

and $a_{2\mu}$ denotes the characteristic values of the Mathieu functions that depend on the purely imaginary argument $\mathrm{i}\tau\delta\omega/2$. For small values of the parameter $\tau\delta\omega < 2.9$, all angular eigenvalues k_μ are real. With increasing values of the parameter $\tau\delta\omega$, the angular eigenvalues become pairwise complex conjugated as in detail discussed in [19]. A solution for $g_\mu(r,t)$ can be obtained using a Laplace transform with respect to time t

$$\hat{g}_\mu(r,s) = \int_0^\infty \mathrm{d}t \mathrm{e}^{-st} g_\mu(r,t) \tag{12}$$

and a Neumann-Weber transform with respect to radius r [25,26]:

$$\bar{\hat{g}}_\mu(z,s) = \int_R^\infty \mathrm{d}r r \hat{g}_\mu(r,s) \frac{J_{k_\mu}\left(\frac{r}{R}z\right) Y'_{k_\mu}(z) - Y_{k_\mu}\left(\frac{r}{R}z\right) J'_{k_\mu}(z)}{R^2}, \tag{13}$$

where J, Y, J', Y' denotes Bessel functions of the first and second kind and their derivatives, respectively. Applying these both transforms, one obtains:

$$\bar{\hat{g}}_\mu(z,s) = -A_0^{(2\mu)} \frac{S'_{1,k_\mu}(z)}{\pi z^2} \frac{4}{s + Dz^2}, \tag{14}$$

where $A_0^{(2\mu)}$ are the Fourier coefficients of the Mathieu functions as given in Eq. (B2) in Appendix B and $S'_{1,k_\mu}(z)$ denotes Lommel function derivatives [27]. Details of this calculation are provided in Appendix B. The original eigenfunction $g_\mu(r,t)$ are yielded by an inverse Neumann-Weber transform and an inverse Laplace transform.

Finally, the local magnetization $m(r,\phi,t)$ around a single cylindrical vessel can be written as:

$$\begin{aligned}\frac{m(r,\phi,t)}{m_0} = {} & \frac{4}{\pi}\sum_{\mu=0}^{\infty} A_0^{(2\mu)} \mathrm{ce}_{2\mu}\left(\phi, \mathrm{i}\frac{\tau\delta\omega}{2}\right) \\ & \times \left[\int_0^\infty \mathrm{d}z \frac{S'_{1,k_\mu}(z)}{z} \frac{J'_{k_\mu}(z) Y_{k_\mu}(z\frac{r}{R}) - Y'_{k_\mu}(z) J_{k_\mu}(z\frac{r}{R})}{[J'_{k_\mu}(z)]^2 + [Y'_{k_\mu}(z)]^2} \mathrm{e}^{-\frac{t}{\tau}z^2} \right. \\ & \left. + \pi \sum_{\nu=1}^{N_\mu} \frac{z_{\mu\nu} S'_{1,k_\mu}(z_{\mu\nu})}{z_{\mu\nu}^2 - k_\mu^2} \frac{H_{k_\mu}^{(1)}(z_{\mu\nu}\frac{r}{R})}{H_{k_\mu}^{(1)}(z_{\mu\nu})} \mathrm{e}^{-\frac{t}{\tau}z_{\mu\nu}^2}\right],\end{aligned} \tag{15}$$

where $z_{\mu\nu}$ are zeros of the first derivative of the Hankel function of the first kind with $\mathrm{Im}(z_{\mu\nu}) \geqslant 0$:

$$H_{k_\mu}^{(1)\prime}(z_{\mu\nu}) = 0. \tag{16}$$

The number of zeros N_μ depends on the parameter $\tau\delta\omega$ and is visualized in Fig. 2. Details about the zeros $z_{\mu\nu}$ and their numerical implementation are given in Appendix C. The zeros $z_{\mu\nu}$ are visualized as functions of the parameter $\tau\delta\omega$ in Fig. 3.

The relaxation function $f(t)$ can be obtained by putting the local magnetization from Eq. (15) into Eq. (6):

$$\begin{aligned} f(t) = {} & \frac{16}{\pi^2}\sum_{\mu=0}^{\infty}\left[A_0^{(2\mu)}\right]^2 \times \left[\int_0^\infty \frac{\mathrm{d}z}{z^3} \frac{[S'_{1,k_\mu}(z)]^2\left[1 - \frac{t}{\tau}z^2 - \mathrm{e}^{-\frac{t}{\tau}z^2}\right]}{[J'_{k_\mu}(z)]^2 + [Y'_{k_\mu}(z)]^2}\right. \\ & \left. + \mathrm{i}\pi \sum_{\nu=1}^{N_\mu} \frac{[S'_{1,k_\mu}(z_{\mu\nu})]^2\left[1 - \frac{t}{\tau}z_{\mu\nu}^2 - \mathrm{e}^{-\frac{t}{\tau}z_{\mu\nu}^2}\right]}{z_{\mu\nu}[z_{\mu\nu}^2 - k_\mu^2] J'_{k_\mu}(z_{\mu\nu}) H_{k_\mu}^{(1)}(z_{\mu\nu})}\right].\end{aligned} \tag{17}$$

An implementation of the relaxation function in MATHEMATICA® [28] is provided as supplementary material. The relaxation function $f(t)$ exhibits a quadratic behavior for short times as detailed in Appendix D. Interestingly, the quadratic behavior for short times is independent of the vessel radius:

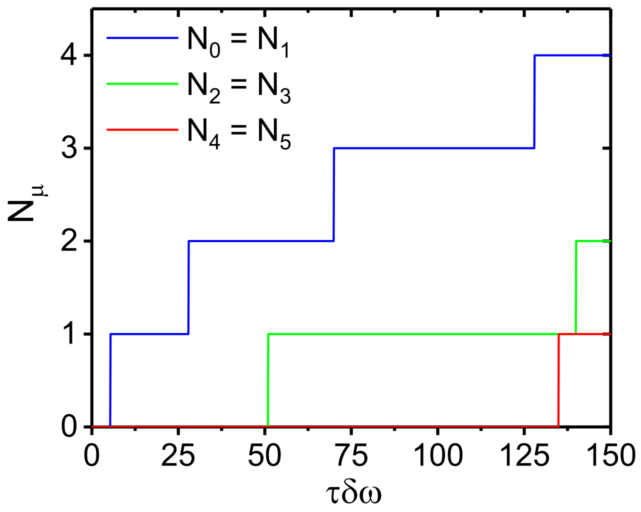

Fig. 2. The number of zeros N_μ of the first derivative of the Hankel function as defined in Eq. (16) in dependence on the parameter $\tau\delta\omega$. The number of zeros N_μ is analyzed in detail in Appendix C, see Fig. 7 and Table 1.

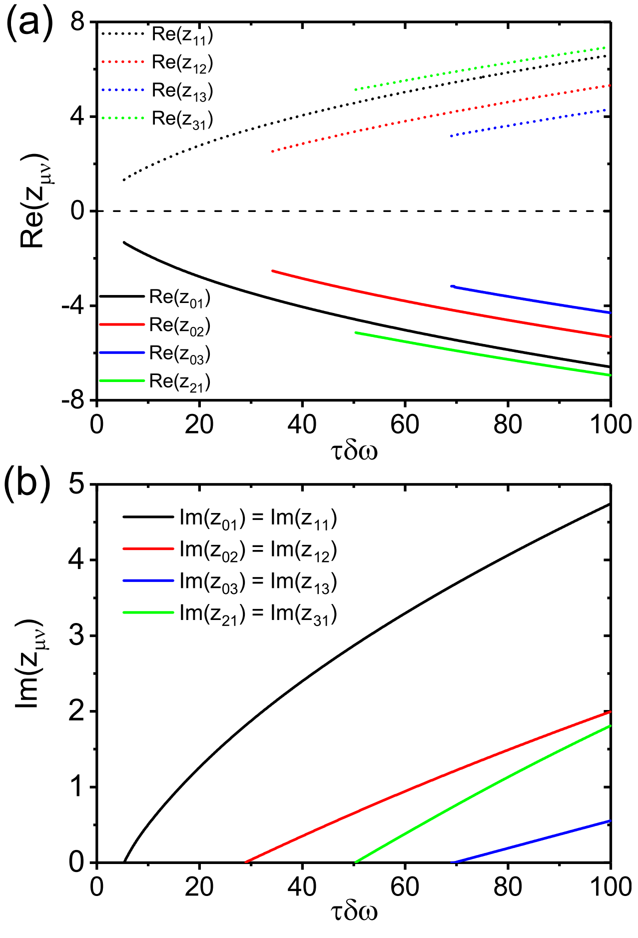

Fig. 3. (a) Real part and (b) imaginary part of the zeros $z_{\mu\nu}$. The zeros exhibit the symmetry $z_{2\mu,\nu} = -z^*_{2\mu+1,\nu}$. With increasing values of the parameter $\tau\delta\omega$, the number of occurring zeros in Eq. (15) increases.

$$f(t) \approx \frac{\delta\omega^2 t^2}{4} \quad \text{for } \delta\omega t \ll 1. \tag{18}$$

This agrees with the short time limit in the static dephasing and motional narrowing limit (see below) [12,13]. For large values of $\tau\delta\omega \gg 1$, the short time limit is applicable up to $\delta\omega t \approx 1$, for small values of $\tau\delta\omega \lesssim 1$, it is only applicable for very short times $\delta\omega t \ll 1$. The long time limit of the relaxation function depends on the diffusion regime. In the static dephasing regime, the relaxation function is linear in time (see Eq. (A13) in [12]), whereas in the motional narrowing regime, the relaxation function shows a $f(t) \sim t\ln(t)$ behavior (see Eq. (25) in [13]). The long time behavior is in detail analyzed in Appendix D. Finally, the relaxation function for long times can be obtained as:

$$\begin{aligned} f(t) = {} & \frac{16}{\pi^2}\frac{t}{\tau}\left[\int_0^\infty \mathrm{d}z \ln(z) \sum_{\mu=0}^{\infty}\left[A_0^{(2\mu)}\right]^2 D_{k_\mu}(z)\right. \\ & \left. + \mathrm{i}\sum_{\nu=1}^{N_\mu} \frac{\pi z_{\mu\nu}[S'_{1,k_\mu}(z_{\mu\nu})]^2}{[k_\mu^2 - z_{\mu\nu}^2] J'_{k_\mu}(z_{\mu\nu}) H_{k_\mu}^{(1)}(z_{\mu\nu})}\right] \\ & - \left[A_0^{(0)}\right]^2 \left[\frac{4t}{\tau}\right]^{1-k_0} \frac{\pi k_0 \mathrm{e}^{-k_0[1-\tilde{\gamma}]}}{[1+k_0][\Gamma(k_0)]^2} \cot\left(\frac{\pi k_0}{2}\right),\end{aligned} \tag{19}$$

where $D_{k_\mu}(z)$ is defined in Appendix D and $\tilde{\gamma} \approx 0.57722$ is Euler's constant. The first two terms of the relaxation function grow linearly in time, the third term depends on the first angular eigenvalue k_0: for $\tau\delta\omega \lesssim 2.5$, the first angular eigenvalue is smaller than $k_0 < 1$ and the third term significantly decreases the relaxation function for long times. For $\tau\delta\omega > 2.5$, the third term is negligible for long times. Details about the asymptotic behavior of the relaxation function are provided in Appendix D.

In a gradient echo experiment, relaxation rates R_2^* are often acquired with a single echo time TE. The determined relaxation rates R_2^* then depend on the echo time TE and are closely connected to the relaxation function:

$$R_2^* = -\frac{1}{\mathrm{TE}} \ln\left(\frac{M(\mathrm{TE})}{M_0}\right) = \eta \frac{f(\mathrm{TE})}{\mathrm{TE}}. \tag{20}$$

The relaxation rate R_2^* is shown in Fig. 4 as a function of the echo time TE for different values of the parameter $\tau\delta\omega$. For short times, the relaxation rate grows linearly with the echo time as given by Eqs. (18) and (20). In Fig. 5, the relaxation rate R_2^* is shown as a function of the parameter $\tau\delta\omega$ and compared with limiting regimes and simulation data.

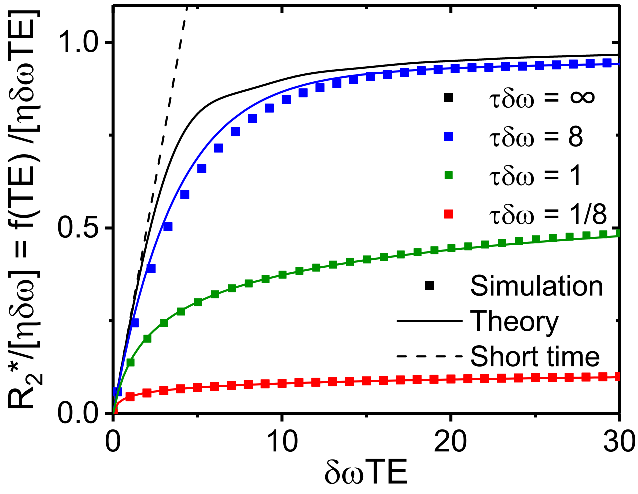

Fig. 4. Relaxation rate R_2^* according to Eqs. (20) and (17) in dependence on the echo time TE for different diffusion strength. For short times, the relaxation rate increases linearly as shown in the black dashed line $R_2^* = \eta\delta\omega^2\mathrm{TE}/4$. For small parameter $\tau\delta\omega$, this coincidence is restricted to very short times $\delta\omega t \ll 1$. The long time limit depends on the parameter $\tau\delta\omega$. Numerical simulations shown as squares coincide very well with theoretical predictions in the solid lines. The static dephasing limit is obtained from Eq. (22) and shown as black solid line.

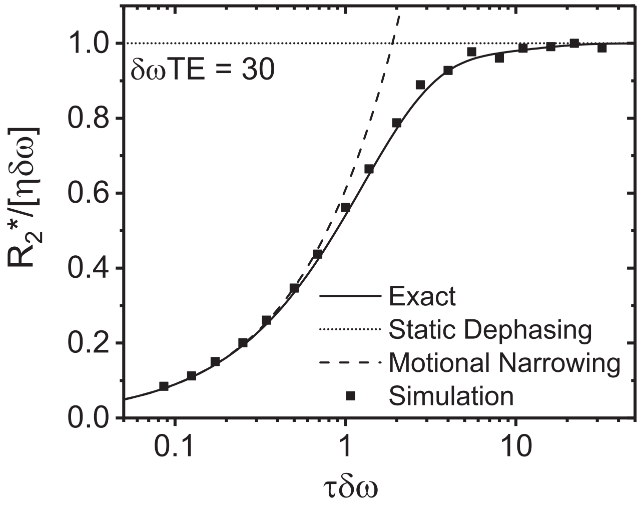

Fig. 5. Relaxation rate R_2^* according to Eq. (20) in dependence on the parameter $\tau\delta\omega$ for a fixed echo time $\delta\omega\mathrm{TE} = 30$. The exact line is obtained from Eq. (20) with $f(t)$ given in Eq. (17), the static dephasing limit from Eq. (22) and the motional narrowing limit from Eq. (21).

4. Validation

In the motional narrowing limit $\tau\delta\omega \to 0$, the sum over v in Eq. (17) vanishes since no zeros are present. The first addend in the infinite sum with $\mu = 0$ vanishes as well since $S'_{1,0}(z) = 0$. Finally, only the addend with $\mu = 1$ in Eq. (17) contributes to the infinite sum and one obtains:

$$f(t) \approx \left[\frac{4}{\pi}\tau\delta\omega\right]^2 \int_0^\infty \frac{\mathrm{d}z}{z^9} \frac{\exp\left(-\frac{t}{\tau}z^2\right) + \frac{t}{\tau}z^2 - 1}{\left[J_2'(z)\right]^2 + \left[Y_2'(z)\right]^2}, \tag{21}$$

which agrees with Eq. (22) in [13].

In the static dephasing regime $\tau\delta\omega \to \infty$, the relaxation function $f(t)$ coincides with the results of Yablonskiy and Haacke [12]:

$$f(t) = {}_1F_2\left(-\frac{1}{2}; \frac{1}{2}, 1 \middle| -\frac{\delta\omega^2 t^2}{4}\right) - 1, \tag{22}$$

where ${}_1F_2$ denotes the extended hypergeometric function as defined in Eqs. (13)–(15) in [29].

The final results agree very well with random walk simulations as shown in Figs. 4 and 5. Random walk simulations were performed with 10 different vessel configurations per data point of each time $K = 1800$ randomly arranged parallel cylindrical vessels. The volume fraction $\eta = 0.02$ was fixed. For each configuration 10,000 random walk trajectories were simulated with a step size of $\sqrt{2D\Delta t} = R/4$. Details of the algorithm are presented in [14].

5. Summary and conclusion

The signal evolution around microscopic vessel networks is characterized by the interplay between magnetic field inhomogeneities as well as diffusion effects. Both effects are mathematically treated with the Bloch-Torrey equation. The Bloch-Torrey equation is typically analyzed for a linear gradient [20,30], which is essential for the description of diffusion weighted imaging [31]. Stoller et al. analyzed the Bloch-Torrey equation for a linear gradient for unbounded diffusion as well as diffusion between two boundaries [32]. The Bloch-Torrey equation for a linear gradient for two- and three-dimensional objects are *e.g.* analyzed in [33]. Numerous of mathematical and numerical details of the Bloch-Torrey equation for a linear gradient were analyzed by Grebenkov et al., *e.g.* [34–39]. Besides the linear gradient, there are only a few object geometries and related Larmor frequencies for which the Bloch-Torrey equation can analytically be solved [40–42] as the diffusion in a three-dimensional dipole field on the surface of a sphere [43]. In this work, the Bloch-Torrey equation is for the first time exactly solved for unbounded diffusion around a single vessel that creates a two-dimensional dipole field as given in Eq. (2). In the contrary, previous works were limited to the motional narrowing or strong dephasing regime [44–46] or replaced the diffusion operator by a similar Markov operator [47–49].

Compared to Krogh's capillary model, where the Bloch-Torrey equation for a single vessel in a dephasing cylinder is exactly solved [19], no outer boundaries are assumed in this work. Thus, the radial eigenvalues become continuous and a Laplace transform of the radial eigenfunctions is convenient. The resulting inhomogeneous modified Bessel differential equation can be solved using a Neumann-Weber transform with respect to r as previously applied in [25]. However, in our work, the Bessel indices k_μ are in general complex and, thus, one has to consider the Neumann-Weber transform for complex indices. The local magnetization can finally be obtained in the form of Eq. (15), where a sum over zeros of Hankel function derivatives occurs. The number of zeros N_μ depends on the interplay between diffusion and susceptibility effects, *e.g.* for strong diffusion $\tau\delta\omega < 5.4$, the sum vanishes. With increasing values of the parameter $\tau\delta\omega$, the number of zeros increases as shown in Fig. 2, since more and more angular eigenvalues k_μ become complex valued, see Fig. 7 in Appendix C for details.

The statistical approach of Yablonskiy and Haacke, that relates the signal evolution around a single vessel with the signal evolution around randomly arranged parallel vessels, was generalized to arbitrary diffusion strength, see Eq. (7). For this purpose, a linear term in time was added compared to the static dephasing limit. With the operator notation $m(\mathbf{r},t) = \exp(Dt\Delta - \mathrm{i}\omega(\mathbf{r})t)m_0$ that follows from the Bloch-Torrey equation (3), this linear term is given as $Dt\Delta - \mathrm{i}\omega(\mathbf{r})t$ and it becomes clear that the spatial average of this term vanishes in all diffusion regimes since $\langle\omega(\mathbf{r})\rangle = 0$ and m_0 is constant. However, this term guarantees that the integral in Eq. (7) converges properly as shown in Appendix A.

The final expression for the relaxation function $f(t)$ agrees in the regime of strong diffusion with the results of Sukstanskii and Yablonskiy [13]. This is remarkable since the original Eq. (6) was assumed to be valid in the regime of weak diffusion. In general, the function $f(t)$ behaves in a typical manner, as it grows quadratically for short times and shows a more complicated growth for long times: for large vessel diameter, the relaxation function grows linearly in time, for small vessel diameter, a second term decreases the relaxation function, whose exponent is determined by the parameter $\tau\delta\omega$. The relaxation rate R_2^* can be determined by a single echo time TE and is closely connected to the relaxation function $f(t)$ as shown in Eq. (20). The relaxation rate obviously depends on the echo time TE. A comparison between random walk simulation and our theory shows a very good agreement for arbitrary vessel diameters and diffusion strengths, see Figs. 4 and 5.

The results are therefore highly relevant for vessel size imaging, where so far only the static dephasing regime was used as description of the gradient echo relaxation rate [9,10] and, thus, strong susceptibility effects were necessary to justify this assumption (see *e.g.* Fig. 2 in [50]). However, with a complete description of the gradient echo relaxation rate, smaller susceptibility effects allow reaching an optimal sensitivity in the ratio R_2/R_2^* in dependence on the vessel size, see *e.g.* Fig. 3 in [49] or Fig. 6 in [46].

The same argumentation applies for vessel architectural imaging, which has so far only been qualitatively analyzed. However, with this expression for the gradient echo relaxation rate and an appropriate expression for the spin echo relaxation rate, a quantitative analysis of vessel architectural imaging might be possible.

In conclusion, we provided an exact solution of the Bloch-Torrey equation around a single vessel for arbitrary vessel diameters. Generalizing the connection to the static dephasing limit, we obtained the gradient echo signal around uniformly distributed parallel vessels for arbitrary diffusion strength.

Acknowledgments

This work was supported by grants from the Deutsche Forschungsgemeinschaft (Contract Grant No.: DFG ZI 1295/2-1 and DFG KU 3555/1-1). L.R. Buschle was supported by Studienstiftung des Deutschen Volkes.

Appendix A. Averaging over randomly arranged parallel vessels

The local magnetization around uniformly distributed parallel vessels is determined by the Bloch-Torrey equation:

$$\frac{\partial}{\partial t} m(\mathbf{r},t) = \left[D\Delta - \mathrm{i}\sum_{i=1}^{K}\omega_l(\mathbf{r}-\mathbf{r}_i)\right] m(\mathbf{r},t), \tag{A1}$$

where $\mathbf{r}_i$ are random positions of the vessels $i = 1\ldots K$. This equation is formally solved by the operator exponential

$$m(\mathbf{r},t) = \exp\left(Dt\Delta - \mathrm{i}t\sum_{i=1}^{K}\omega_l(\mathbf{r}-\mathbf{r}_i)\right)m_0. \tag{A2}$$

The signal $M(t)$ is then obtained as a superposition of the local magnetization over the voxel V excluding the area ηV of vessels

$$\frac{M(t)}{M_0} = \left\langle \int_{V-\eta V} \mathrm{d}^2\mathbf{r} \frac{\exp\left(Dt\Delta - \mathrm{i}t\sum_{i=1}^{K}\omega_l(\mathbf{r}-\mathbf{r}_i)\right)1}{V-\eta V}\right\rangle_{\text{position}} \tag{A3}$$

and $\langle\ldots\rangle_{\text{position}}$ denotes averaging over the random positions $\mathbf{r}_1, \mathbf{r}_2, \ldots, \mathbf{r}_K$ of the vessels. Since uniformly distributed parallel vessels are assumed, the averaging over the positions can be performed:

$$\frac{M(t)}{M_0} = \prod_{j=1}^{K}\int_{V-\eta V}\frac{\mathrm{d}^2\mathbf{r}_j}{V-\eta V}\exp\left(Dt\Delta - \mathrm{i}t\sum_{i=1}^{K}\omega_l(\mathbf{r}_i)\right)1, \tag{A4}$$

where the expression becomes independent of the position $\mathbf{r}$ by averaging over all vessel positions $\mathbf{r}_j$ [23]. It is convenient to rewrite the diffusion operator $D\Delta$ as a sum of local diffusion operators that only act in the neighborhood of the vessel position. A small volume fraction η then justifies factorization of the exponential function. In a physical view, dephasing is treated in analogy to the work of Yablonskiy and Haacke [12], so that in the static dephasing limit the influence of the overlapping dipole fields on the magnetization is correctly described. The diffusion process, however, is only considered in a neighborhood of the closest capillary. This corresponds to an approximation in the lowest order of the blood volume fraction η. Thus, the signal can be expressed as the magnetization of a single vessel to the power of K:

$$\frac{M(t)}{M_0} = \left[\int_{|\mathbf{r}|>R}\frac{\mathrm{d}^2\mathbf{r}}{V[1-\eta]}\exp(Dt\Delta - \mathrm{i}t\omega_l(\mathbf{r}))1\right]^K. \tag{A5}$$

With the relaxation function f defined in Eq. (6), the signal can be rewritten in the form:

$$\frac{M(t)}{M_0} = \left[1 - \frac{\eta}{K}f(t)\right]^K. \tag{A6}$$

In the limit $V, K \to \infty$ and $\pi R^2 K/V = \eta = \text{const.}$, the signal becomes:

$$\frac{M(t)}{M_0} = \exp(-\eta f(t)). \tag{A7}$$

Thus, the signal evolution around randomly distributed parallel vessels is determined by the signal evolution around a single vessel. The relaxation function $f(t)$ can be found as:

$$f(t) = \frac{1}{\pi R^2}\int_{|\mathbf{r}|>R}\mathrm{d}^2\mathbf{r}[1 - \exp(Dt\Delta - \mathrm{i}t\omega_l(\mathbf{r}))]. \tag{A8}$$

A formal power series expansion of the exponential function reveals:

$$f(t) = -\frac{1}{\pi R^2}\int_{|\mathbf{r}|>R}\mathrm{d}^2\mathbf{r}\left[[D\Delta - \mathrm{i}\omega_l(\mathbf{r})]t + \sum_{k=2}^{\infty}[D\Delta - \mathrm{i}\omega_l(\mathbf{r})]^k\frac{t^k}{k!}\right]. \tag{A9}$$

Since $[D\Delta - \mathrm{i}\omega_l(\mathbf{r})] \propto r^{-2}$ decreases quadratically with increasing radii, the convergence of the integral over the sum is obvious. The integral over the linear term in time $[D\Delta - \mathrm{i}\omega_l(\mathbf{r})]t$ would in principle diverge, however, it becomes zero since $\langle\omega_l(\mathbf{r})\rangle = 0$. To ensure that the relaxation function converges properly, it is convenient to subtract the zero-term $[D\Delta - \mathrm{i}\omega_l(\mathbf{r})]t$. Rewriting the expression in terms of the local magnetization, one arrives at Eq. (7).

Appendix B. Radial eigenfunctions of the local magnetization

We consider the Bloch-Torrey equation around a single vessel. The local magnetization can be obtained by a separation ansatz as given in Eq. (9). The angular eigenfunctions are given as Mathieu functions and the radial eigenfunctions $g_\mu(r,t)$ have to fulfill Eq. (10). Since the Bloch-Torrey equation has to be solved on an unbounded domain $R \leqslant r < \infty$, the radial eigenvalues are continuous. Thus, it is convenient to apply a Laplace transform in time domain. Eq. (10) transforms into:

$$\left[\frac{\partial^2}{\partial r^2}+\frac{1}{r}\frac{\partial}{\partial r}-\frac{s}{D}-\frac{k_\mu^2}{r^2}\right]\hat{g}_\mu(r,s) = -2\frac{A_0^{(2\mu)}}{D}, \tag{B1}$$

where the Fourier coefficients $A_0^{(2\mu)}$ are given as

$$A_0^{(2\mu)} = \frac{1}{2\pi}\int_0^{2\pi} \mathrm{d}\phi\, \mathrm{ce}_{2\mu}\left(\phi, \mathrm{i}\frac{\tau\delta\omega}{2}\right). \tag{B2}$$

Eq. (B1) can be solved by a Neumann-Weber transform as given in Eq. (13), see also Eq. (2.4.12) on page 27 in [25]. One arrives at:

$$-z^2\bar{\hat{g}}_\mu(z,s) = \frac{s}{D}\bar{\hat{g}}_\mu(z,s) + \frac{4}{\pi}\frac{A_0^{(2\mu)}}{D}\frac{S'_{1,k_\mu}(z)}{z^2}, \tag{B3}$$

where we used the Lommel integral given in Eq. (5) in section 10.74 on page 350 in [51]. The solution $\bar{\hat{g}}_\mu(z,s)$ is given in Eq. (14). The radial eigenfunctions can be obtained by an inverse Laplace transform with respect to s and an inverse Neumann-Weber transform with respect to z. The inverse Laplace transform is straightforward and yields:

$$\bar{g}_\mu(z,t) = -\frac{4}{\pi}A_0^{(2\mu)}\frac{S'_{1,k_\mu}(z)}{z^2}\mathrm{e}^{-Dtz^2}. \tag{B4}$$

The inverse Neumann-Weber transform for complex indices k_μ is given as:

$$\begin{aligned} g_\mu(r,t) = {} & \pi\sum_{\nu=1}^{N_\mu} z_{\mu\nu}^3 \frac{\bar{g}_\mu(z_{\mu\nu},t)}{k_\mu^2 - z_{\mu\nu}^2}\frac{H^{(1)}_{k_\mu}(\frac{r}{R}z_{\mu\nu})}{H^{(1)}_{k_\mu}(z_{\mu\nu})} \\ & + \int_0^\infty \mathrm{d}z\bar{g}_\mu(z,t)z\frac{J_{k_\mu}(\frac{r}{R}z)Y'_{k_\mu}(z) - Y_{k_\mu}(\frac{r}{R}z)J'_{k_\mu}(z)}{[J'_{k_\mu}(z)]^2 + [Y'_{k_\mu}(z)]^2}, \end{aligned} \tag{B5}$$

where $z_{\mu\nu}$ are complex zeros of the Hankel function derivative as defined in Eq. (16). Putting Eqs. (B4), (B5) and the separation ansatz given in Eq. (9) together, the local magnetization $m(r,\phi,t)$ can be obtained as given in Eq. (15).

In Fig. 6, the radial dependence of the local magnetization is compared with the radial dependence of the local magnetization in Krogh's vessel model [52], where an artificial concentric cylinder with radius R_D with reflecting boundaries is assumed. The local magnetization in Krogh's model was obtained from Eqs. (11) and (20) in [19]. For large radii of the Krogh cylinder ($R_D \gg R$), the local magnetization at the outer boundary is nearly unaffected by the field inhomogeneity of the vessel ($m(r = R_D, \phi, t) \approx m_0$, see blue line in Fig. 6). In this limit, Krogh's model and the exact solution agree very well.

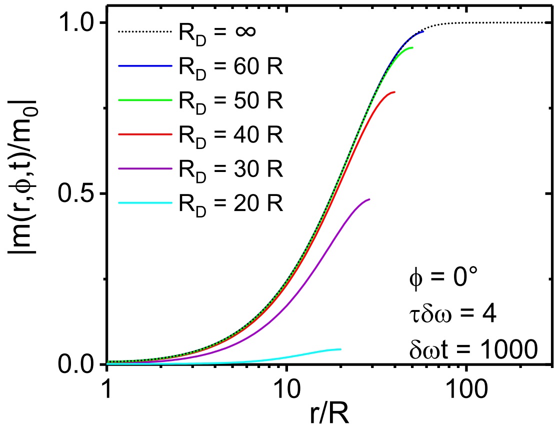

Fig. 6. Absolute value of the local magnetization $|m(\mathbf{r},t)|$ around a single vessel for $\tau\delta\omega = 4$ and $\delta\omega t = 1000$ (dotted line obtained from Eq. (15)) in comparison with Krogh's vessel model (solid lines obtained from Eqs. (11) and (20) in [19]). In Krogh's vessel model, an artificial outer boundary R_D with reflecting boundary conditions exists [19]. If the local magnetization at this outer boundary is nearly unaffected by the field inhomogeneity of the vessel ($m(r = R_D, \phi, t) \approx m_0$, see blue line), Krogh's model leads to similar results than the exact solution (black line). (For interpretation of the references to color in this figure legend, the reader is referred to the web version of this article.)

Appendix C. Numerical determination of $z_{\mu\nu}$

The local magnetization $m(r,\phi,t)$ as well as the relaxation function $f(t)$ depend on the zeros $z_{\mu\nu}$ as defined in Eq. (16). For the analysis of the zeros, it is convenient to analyze the indices k_μ of the derivative of the Hankel function in dependence on the parameter $\tau\delta\omega$. For small values of the parameter $\tau\delta\omega$, the angular eigenvalues k_μ are purely real. With increasing values of the parameter $\tau\delta\omega$, the angular eigenvalues k_μ become pairwise complex conjugated. The positions of the angular eigenvalues k_μ in the complex plane are visualized in Fig. 7 in a parametric plot for increasing values of the parameter $\tau\delta\omega$.

The positions of the indices k_μ determine the number N_μ of occurring zeros and are visualized in Fig. 7 by different background colors: for small values of the parameter $\tau\delta\omega < 2.9$, the indices k_μ of the Hankel derivative are purely real for all summation indices μ and, thus, the Hankel derivative exhibits no zeros in the upper part

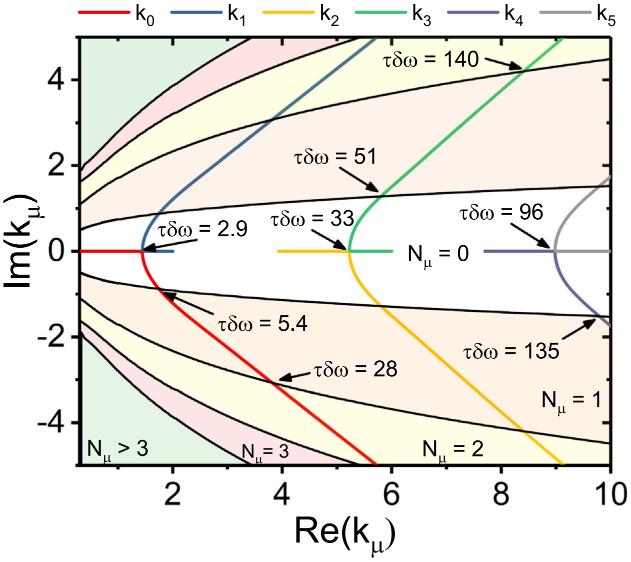

Fig. 7. The number of zeros of the first derivative of the Hankel function as defined in Eq. (16) depends on the position of the angular eigenvalues k_μ in the complex plane. For small vessel diameter ($\tau\delta\omega < 2.9$) all Bessel indices k_μ are real. With increasing values of the parameter $\tau\delta\omega$, the eigenvalues become pair-wise complex conjugated. For $\tau\delta\omega > 2.9$, the eigenvalues k_0 and k_1 are complex conjugated, for $\tau\delta\omega > 33$, the eigenvalues k_2 and k_3 become complex conjugated, etc. The number of zeros N_μ is shown by the background color, *i.e.* white symbolizes $N_\mu = 0$, orange symbolizes $N_\mu = 1$, yellow represents $N_\mu = 2$, etc. Thus, for $5.4 < \tau\delta\omega < 28$ zeros for $\mu = 0$ and $\mu = 1$ occur, *i.e.* $N_0 = N_1 = 1$ (see also Fig. 2). With increasing values of $\tau\delta\omega$, the number of zeros increases as well. (For interpretation of the references to color in this figure legend, the reader is referred to the web version of this article.)

of the complex plane, *e.g.* $N_\mu = 0$. With increasing values of the parameter $2.9 < \tau\delta\omega < 5.4$, the indices k_0, k_1 become complex conjugated. However, the Hankel derivative exhibits no zero in the upper complex plane as well. In Fig. 7, this corresponds to the situation, where the red and blue line are complex conjugated but remain in the white colored area where $N_\mu = 0$. Only for $\tau\delta\omega > 5.4$, zeros for $\mu = 0$ and $\mu = 1$ exist $(N_0, N_1 > 0)$. With increasing values of $\tau\delta\omega$, the number of zeros increases. For $\tau\delta\omega > 33$, the indices k_2 and k_3 become complex conjugated as well and for $\tau\delta\omega > 51$, corresponding zeros z_{21} and z_{31} contribute to the sum in Eq. (15), *i.e.* $N_2, N_3 > 0$.

For numerical determination of the zeros $z_{\mu\nu}$ it is advantageous to use the complex conjugation of the angular eigenvalues $k_{2\mu} = k^*_{2\mu+1}$, if $k_{2\mu}$ is not purely real. Finally, one obtains the symmetry of the zeros:

$$z_{2\mu,\nu} = -z^*_{2\mu+1,\nu}, \tag{C1}$$

see also Fig. 3.

For numerical implementation of the zeros $z_{\mu\nu}$, it is advantageous to use Table 1 as initial values of the root algorithm. There, the zeros are approximated as $\mathrm{Re}(z_{\mu\nu}) \approx A\tau\delta\omega^\alpha$ and $\mathrm{Im}(z_{\mu\nu}) \approx B\tau\delta\omega^\beta + C$, respectively.

The accuracy of the determined zeros can be evaluated using the identity:

$$\begin{aligned}\frac{1}{2} = &\sum_{\nu=1}^{N_\mu} z_{\mu\nu} \frac{S'_{1,k_\mu}(z_{\mu\nu})}{z_{\mu\nu}^2 - k_\mu^2} \frac{H^{(1)}_{k_\mu}(\frac{r}{R} z_{\mu\nu})}{H^{(1)}_{k_\mu}(z_{\mu\nu})} \\ &+ \int_0^\infty \mathrm{d}z \frac{S'_{1,k_\mu}(z)}{\pi z} \frac{Y_{k_\mu}(\frac{r}{R}z)J'_{k_\mu}(z) - J_{k_\mu}(\frac{r}{R}z)Y'_{k_\mu}(z)}{[J'_{k_\mu}(z)]^2 + [Y'_{k_\mu}(z)]^2},\end{aligned} \tag{C2}$$

which needs to be valid for every $R \leqslant r < \infty$ and every index $\mu \in \mathbb{N}_0$. Especially for $r = R$, one finds with $Y_{k_\mu}(z)J'_{k_\mu}(z) - J_{k_\mu}(z)Y'_{k_\mu}(z) = -2/[\pi z]$ the expression

$$\sum_{\nu=1}^{N_\mu} z_{\mu\nu} \frac{S'_{1,k_\mu}(z_{\mu\nu})}{z_{\mu\nu}^2 - k_\mu^2} = \frac{1}{2} + \frac{2}{\pi^2} \int_0^\infty \frac{\mathrm{d}z}{z^2} \frac{S'_{1,k_\mu}(z)}{[J'_{k_\mu}(z)]^2 + [Y'_{k_\mu}(z)]^2} \tag{C3}$$

that can also be used to evaluate the numerical accuracy. An implementation of the relaxation function $f(t)$, the local magnetization $m(r, \phi, t)$ and the zeros $z_{\mu\nu}$ in MATHEMATICA® [28] is provided as supplementary material.

Appendix D. Asymptotic behavior of the relaxation rate

The relaxation function $f(\mathrm{TE})$ given in Eq. (17) and the relaxation rate $R_2^*(\mathrm{TE})$ given in Eq. (20) strongly depend on the echo time TE. The short time behavior can be obtained by a power expansion of the exponential functions that reveals:

$$\begin{aligned}f(t) = -\frac{8}{\pi^2} \frac{t^2}{\tau^2} \sum_{\mu=0}^{\infty} \left[A_0^{(2\mu)}\right]^2 \Bigg[&\int_0^\infty \mathrm{d}z \frac{z[S'_{1,k_\mu}(z)]^2}{[J'_{k_\mu}(z)]^2 + [Y'_{k_\mu}(z)]^2} \\ &+ \mathrm{i}\pi \sum_{\nu=1}^{N_\mu} \frac{z_{\mu\nu}^3}{z_{\mu\nu}^2 - k_\mu^2} \frac{[S'_{1,k_\mu}(z_{\mu\nu})]^2}{J'_{k_\mu}(z_{\mu\nu}) H^{(1)}_{k_\mu}(z_{\mu\nu})} \Bigg].\end{aligned} \tag{D1}$$

The integral in the first line and the sum in the second line can be evaluated by using general properties of the Neumann-Weber transform [53] and one arrives at:

$$f(t) = -\frac{t^2}{\tau^2} \sum_{\mu=0}^{\infty} \left[A_0^{(2\mu)}\right]^2 k_\mu^4. \tag{D2}$$

We use the identity $2A_0^{(2\mu)} k_\mu^2 = \mathrm{i}\tau\delta\omega A_2^{(2\mu)}$ given in Eq. (A.5) in [19] to arrive at:

$$f(t) = \frac{\delta\omega^2 t^2}{4} \sum_{\mu=0}^{\infty} \left[A_2^{(2\mu)}\right]^2. \tag{D3}$$

The last sum is equal to 1 as given in Eq. (13) in [19] and one obtains the final expression presented in Eq. (18).

To analyze the long time behavior of the relaxation function, it is convenient to focus on the integral in Eq. (17) and perform a partial integration. The upper boundary term obviously vanishes. The lower boundary term becomes zero as well, where we used Eq. (A5) in [54] and Eq. (11) in [24] to prove that $\sum_{\mu=0}^{\infty} [A_0^{(2\mu)}]^2 k_\mu^2 = 0$. Replacing the angular eigenvalues by the characteristic value according to Eq. (11) leads to the general valid expression:

$$\sum_{\mu=0}^{\infty} [A_0^{(2\mu)}]^2 a_{2\mu}\left(\mathrm{i}\frac{\tau\delta\omega}{2}\right) = 0, \tag{D4}$$

Table 1

Approximation of the zeros $\mathrm{Re}(z_{\mu\nu}) \approx A\tau\delta\omega^\alpha$ and $\mathrm{Im}(z_{\mu\nu}) \approx B\tau\delta\omega^\beta + C$. The zeros occur for $\tau\delta\omega > \tau\delta\omega_{\min}$. Zeros with odd index μ can be obtained from Eq. (C1).

$\mu = 0$	z_{01}	z_{02}	z_{03}	z_{04}	z_{05}
$\tau\delta\omega_{\min}$	5.4	28	70	128	203
A	−0.625	−0.376	−0.233	−0.129	−0.116
α	0.513	0.578	0.642	0.724	0.723
B	0.628	0.301	0.146	0.0814	0.0923
β	0.505	0.580	0.658	0.717	0.678
C	−1.624	−2.322	−2.476	−2.680	−3.429
$\mu = 2$	z_{21}	z_{22}	z_{23}		
$\tau\delta\omega_{\min}$	51	140	214		
A	−0.756	−0.409	−0.260		
α	0.482	0.563	0.620		
B	0.788	0.551	0.537		
β	0.476	0.500	0.485		
C	−5.230	−6.267	−7.263		
$\mu = 4$	z_{41}				
$\tau\delta\omega_{\min}$	135				
A	−1.121				
α	0.422				
B	0.946				
β	0.431				
C	−5.114				

which agrees with Eqs. (21) and (22) in [41]. Finally, one arrives at:

$$f(t)=\frac{8}{\pi^2}\frac{t}{\tau}\sum_{\mu=0}^{\infty}\left[A_0^{(2\mu)}\right]^2\int_0^{\infty}\mathrm{d}z\left[\frac{\tau}{t}\frac{1-\mathrm{e}^{-\frac{t}{\tau}z^2}}{z^2}-\mathrm{Ei}\left(-\frac{t}{\tau}z^2\right)+2\ln(z)\right]D_{k_\mu}(z),\tag{D5}$$

where

$$D_{k_\mu}(z)=\frac{\mathrm{d}}{\mathrm{d}z}\frac{\left[S'_{1,k_\mu}(z)\right]^2}{\left[J'_{k_\mu}(z)\right]^2+\left[Y'_{k_\mu}(z)\right]^2}.\tag{D6}$$

The integrand in Eq. (D5) can be approximated as:

$$\begin{aligned}&\frac{\tau}{t}\frac{1-\mathrm{e}^{-\frac{t}{\tau}z^2}}{z^2}-\mathrm{Ei}\left(-\frac{t}{\tau}z^2\right)+2\ln(z)\\&\quad\approx\begin{cases}1-\tilde{\gamma}-\ln\left(\frac{t}{\tau}\right) & \text{for } z^2\frac{t}{\tau}<\exp(1-\tilde{\gamma})\\ 2\ln(z) & \text{for } z^2\frac{t}{\tau}\geqslant\exp(1-\tilde{\gamma}).\end{cases}\end{aligned}\tag{D7}$$

Using this approximation, the relaxation function can be obtained as:

$$\begin{aligned}f(t)\approx&\frac{16}{\pi^2}\frac{t}{\tau}\int_0^{\infty}\mathrm{d}z\ln(z)\sum_{\mu=0}^{\infty}\left[A_0^{(2\mu)}\right]^2D_{k_\mu}(z)\\&+\frac{8}{\pi^2}\frac{t}{\tau}\int_0^{\sqrt{\frac{\tau}{t}}\mathrm{e}^{-\frac{\tilde{\gamma}-1}{2}}}\mathrm{d}z\sum_{\mu=0}^{\infty}\left[A_0^{(2\mu)}\right]^2D_{k_\mu}(z)\left[1-\tilde{\gamma}-\ln\left(\frac{t}{\tau}z^2\right)\right].\end{aligned}\tag{D8}$$

It is convenient to analyze the second term in more detail. Therefore, one needs the asymptotic behavior of $D_{k_\mu}(z)$ for small values of the parameter z:

$$D_{k_\mu}(z)\approx-\frac{\pi^2k_\mu^2}{2}\cot\left(\frac{\pi k_\mu}{2}\right)\frac{\mathrm{d}}{\mathrm{d}z}\frac{J'_{k_\mu}(z)}{Y'_{k_\mu}(z)}\tag{D9}$$

$$\approx-\frac{\pi^3k_\mu^3\cot\left(\frac{\pi k_\mu}{2}\right)}{4^{k_\mu}\left[\Gamma(k_\mu)\right]^2\left[1+k_\mu\right]}z^{2k_\mu-1}.\tag{D10}$$

Putting this approximation into Eq. (D8) and solving the integral, one finds:

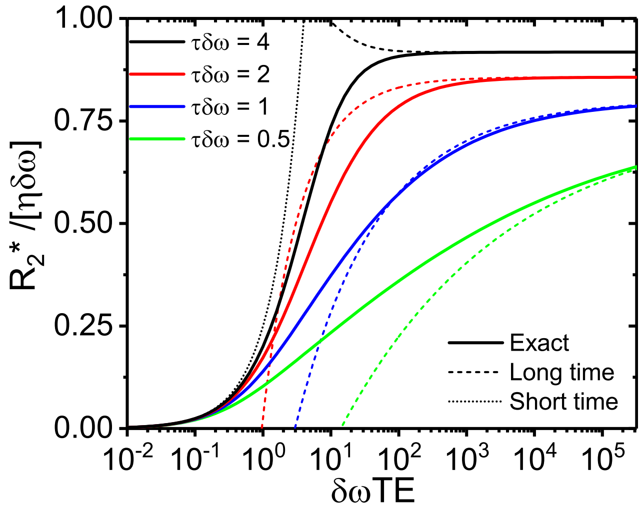

Fig. 8. Comparison of the exact relaxation rate R_2^* obtained from Eqs. (20) and (17) (solid lines) with its short (dotted line) and long time approximations (dashed lines) given in Eqs. (18) and (19) for different values of the parameter $\tau\delta\omega$. For $\tau\delta\omega > 2.5$, the first angular eigenvalue k_0 is greater than 1 and, thus, the relaxation rate is constant for long times and the according long time approximation increases for shorter echo times.

$$\begin{aligned}f(t)=&\frac{16}{\pi^2}\frac{t}{\tau}\int_0^{\infty}\mathrm{d}z\ln(z)\sum_{\mu=0}^{\infty}\left[A_0^{(2\mu)}\right]^2D_{k_\mu}(z)\\&-\pi\sum_{\mu=0}^{\infty}\left[A_0^{(2\mu)}\right]^2\left[\frac{4t}{\tau}\right]^{1-k_\mu}\frac{k_\mu\mathrm{e}^{-k_\mu[\tilde{\gamma}-1]}\cot\left(\frac{\pi k_\mu}{2}\right)}{\left[1+k_\mu\right]\left[\Gamma(k_\mu)\right]^2}.\end{aligned}\tag{D11}$$

Since the angular eigenvalues k_μ are ordered, *i.e.* $k_0 < k_1 < k_2 < \ldots$, the long time behavior is completely determined by the addend in the sum with $\mu = 0$ and one finally arrives at Eq. (19). For $k_0 > 1$ that corresponds to $\tau\delta\omega > 2.5$, the second term does not contribute to the long time behavior and the relaxation function increases linearly. The relaxation rate R_2^* is compared in Fig. 8 with its asymptotic expressions for short and long times.

References

[1] G. Klug, T. Kampf, C. Ziener, M. Parczyk, E. Bauer, V. Herold, E. Rommel, P.M. Jakob, W.R. Bauer, Murine atherosclerotic plaque imaging with the USPIO Ferumoxtran-10, Front. Biosci. (Landmark Ed.) 14 (2009) 2546–2552.

[2] R.B. Buxton, Introduction to Functional Magnetic Resonance Imaging: Principles and Techniques, Cambridge University Press, 2009.

[3] A. Deistung, F. Schweser, J.R. Reichenbach, Overview of quantitative susceptibility mapping, NMR Biomed. 30 (4) (2017) e3569.

[4] D.A. Yablonskiy, Quantitation of intrinsic magnetic susceptibility-related effects in a tissue matrix. Phantom study, Magn. Reson. Med. 39 (3) (1998) 417–428.

[5] X. He, M. Zhu, D.A. Yablonskiy, Validation of oxygen extraction fraction measurement by qBOLD technique, Magn. Reson. Med. 60 (2008) 882–888.

[6] J. Sedlacik, J.R. Reichenbach, Validation of quantitative estimation of tissue oxygen extraction fraction and deoxygenated blood volume fraction in phantom and in vivo experiments by using MRI, Magn. Reson. Med. 63 (4) (2010) 910–921.

[7] R.M. Weisskoff, C.S. Zuo, J.L. Boxerman, B.R. Rosen, Microscopic susceptibility variation and transverse relaxation: theory and experiment, Magn. Reson. Med. 31 (1994) 601–610.

[8] J.L. Boxerman, L.M. Hamberg, B.R. Rosen, R.M. Weisskoff, MR contrast due to intravascular magnetic susceptibility perturbations, Magn. Reson. Med. 34 (1995) 555–566.

[9] I. Troprés, S. Grimault, A. Vaeth, E. Grillon, C. Julien, J.F. Payen, L. Lamalle, M. Decorps, Vessel size imaging, Magn. Reson. Med. 45 (3) (2001) 397–408.

[10] K.E. Emblem, C.T. Farrar, E.R. Gerstner, T.T. Batchelor, R.J.H. Borra, B.R. Rosen, A. G. Sorensen, R.K. Jain, Vessel calibre – a potential MRI biomarker of tumour response in clinical trials, Nat. Rev. Clin. Oncol. 11 (2014) 566–584.

[11] K.E. Emblem, K. Mouridsen, A. Bjornerud, C.T. Farrar, D. Jennings, R.J.H. Borra, P.Y. Wen, P. Ivy, T.T. Batchelor, B.R. Rosen, R.K. Jain, A.G. Sorensen, Vessel architectural imaging identifies cancer patient responders to anti-angiogenic therapy, Nat. Med. 19 (9) (2013) 1178–1183.

[12] D.A. Yablonskiy, E.M. Haacke, Theory of NMR signal behavior in magnetically inhomogeneous tissues: the static dephasing regime, Magn. Reson. Med. 32 (1994) 749–763.

[13] A.L. Sukstanskii, D.A. Yablonskiy, Gaussian approximation in the theory of MR signal formation in the presence of structure-specific magnetic field inhomogeneities. Effects of impermeable susceptibility inclusions, J. Magn. Reson. 167 (2004) 56–67.

[14] F.T. Kurz, C.H. Ziener, M. Rückl, A. Hahn, V.J.F. Sturm, K. Zhang, L.R. Buschle, M. Bendszus, S. Heiland, H.P. Schlemmer, W.R. Bauer, T. Kampf, The influence of spatial patterns of capillary networks on transverse relaxation, Magn. Reson. Imag. 40 (2017) 31–47.

[15] M.O. Breckwoldt, J. Bode, F.T. Kurz, A. Hoffmann, K. Ochs, M. Ott, K. Deumelandt, T. Krüwel, D. Schwarz, M. Fischer, X. Helluy, D. Milford, K. Kirschbaum, G. Solecki, S. Chiblak, A. Abdollahi, F. Winkler, W. Wick, M. Platten, S. Heiland, M. Bendszus, B. Tews, Correlated magnetic resonance imaging and ultramicroscopy (MR-UM) is a tool kit to assess the dynamics of glioma angiogenesis, eLife (2016) e11712.

[16] F.T. Kurz, L.R. Buschle, T. Kampf, K. Zhang, H.P. Schlemmer, S. Heiland, M. Bendszus, C.H. Ziener, Spin dephasing in a magnetic dipole field around large capillaries: approximative and exact results, J. Magn. Reson. 273 (2016) 83–97.

[17] C.H. Ziener, F.T. Kurz, T. Kampf, Free induction decay caused by a dipole field, Phys. Rev. E 91 (2015) 032707.

[18] F.T. Kurz, T. Kampf, L.R. Buschle, H.P. Schlemmer, M. Bendszus, S. Heiland, C.H. Ziener, Generalized moment analysis of magnetic field correlations for accumulations of spherical and cylindrical magnetic perturbers, Front. Phys. 4 (2016) 46.

[19] C.H. Ziener, T. Kampf, G. Reents, H.P. Schlemmer, W.R. Bauer, Spin dephasing in a magnetic dipole field, Phys. Rev. E 85 (2012) 051908.

[20] H.C. Torrey, Bloch equations with diffusion terms, Phys. Rev. 104 (1956) 563–565.

[21] F. Cassot, F. Lauwers, C. Fouard, S. Prohaska, V. Lauwers-Cances, A novel three-dimensional computer-assisted method for a quantitative study of microvascular networks of the human cerebral cortex, Microcirculation 13 (1) (2006) 1–18.

[22] V.G. Kiselev, S. Posse, Analytical theory of susceptibility induced nmr signal dephasing in a cerebrovascular network, Phys. Rev. Lett. 81 (25) (1998) 5696.

[23] V.G. Kiselev, S. Posse, Analytical model of susceptibility-induced MR signal dephasing: effect of diffusion in a microvascular network, Magn. Reson. Med. 41 (1999) 499–509.

[24] C.H. Ziener, M. Rückl, T. Kampf, W.R. Bauer, H.P. Schlemmer, Mathieu functions for purely imaginary parameters, J. Comput. Appl. Math. 236 (2012) 4513–4524.

[25] R.K.M. Thambynayagam, The Diffusion Handbook: Applied Solutions for Engineers, McGraw Hill Professional, 2011.

[26] C.H. Ziener, T. Kampf, F.T. Kurz, Diffusion propagators for hindered diffusion in open geometries, Concepts Magn. Reson. A 44 (2015) 150–159.

[27] C.H. Ziener, F.T. Kurz, L.R. Buschle, T. Kampf, Orthogonality, Lommel integrals and cross product zeros of linear combinations of Bessel functions, SpringerPlus 4 (2015) 390.

[28] S. Wolfram, The Mathematica Book, Cambridge University Press, New York, 1999.

[29] C.H. Ziener, W.R. Bauer, P.M. Jakob, Frequency distribution and signal formation around a vessel, Magn. Reson. Mater. Phys. 18 (2005) 225–230.

[30] E.O. Stejskal, J.E. Tanner, Spin diffusion measurements: spin echoes in the presence of a time-dependent field gradient, J. Chem. Phys. 42 (1) (1965) 288–292.

[31] D. Le Bihan, Molecular diffusion, tissue microdynamics and microstructure, NMR Biomed. 8 (1995) 375–386.

[32] S.D. Stoller, W. Happer, F.J. Dyson, Transverse spin relaxation in inhomogeneous magnetic fields, Phys. Rev. A 44 (1991) 7459–7477.

[33] T.M. de Swiet, P.N. Sen, Decay of nuclear magnetization by bounded diffusion in a constant field gradient, J. Chem. Phys. 100 (8) (1994) 5597–5604.

[34] D.S. Grebenkov, NMR survey of the reflected Brownian motion, Rev. Mod. Phys. 79 (2007) 1077–1137.

[35] D.S. Grebenkov, Exploring diffusion across permeable barriers at high gradients. II. Localization regime, J. Magn. Reson. 248 (2014) 164–176.

[36] D.S. Grebenkov, B. Helffer, R. Henry, The complex Airy operator on the line with a semipermeable barrier, SIAM J. Math. Anal. 49 (3) (2017) 1844–1894.

[37] D.S. Grebenkov, Diffusion MRI/NMR at high gradients: challenges and perspectives, Micropor. Mesopor. Mater. 269 (2018) 79–82.

[38] D.S. Grebenkov, B. Helffer, On spectral properties of the Bloch–Torrey operator in two dimensions, SIAM J. Math. Anal. 50 (1) (2018) 622–676.

[39] Y. Almog, D.S. Grebenkov, B. Helffer, Spectral semi-classical analysis of a complex Schrödinger operator in exterior domains, J. Math. Phys. 59 (4) (2018) 041501.

[40] A. Seeger, The determination of the diffusion coefficient of positive muons from the transverse depolarization in type-II superconductors, Phys. Lett. A 74 (3–4) (1979) 259–262.

[41] A. Seeger, Transverse spin relaxation of spin carriers diffusing in spatially periodic magnetic fields, Hyperfine Interact. 105 (1) (1997) 151–159.

[42] F.T. Kurz, L.R. Buschle, A. Hahn, J.M.E. Jende, M. Bendszus, S. Heiland, C.H. Ziener, Diffusion effects in myelin sheath free induction decay, J. Magn. Reson. 297 (2018) 61–75.

[43] L.R. Buschle, F.T. Kurz, T. Kampf, W.L. Wagner, J. Duerr, W. Stiller, P. Konietzke, F. Wünnemann, M.A. Mall, M.O. Wielpütz, H.P. Schlemmer, C.H. Ziener, Dephasing and diffusion on the alveolar surface, Phys. Rev. E 95 (2-1) (2017) 022415.

[44] J.H. Jensen, R. Chandra, NMR relaxation in tissues with weak magnetic inhomogeneities, Magn. Reson. Med. 44 (2000) 144–156.

[45] C.H. Ziener, T. Kampf, V. Herold, P.M. Jakob, W.R. Bauer, W. Nadler, Frequency autocorrelation function of stochastically fluctuating fields caused by specific magnetic field inhomogeneities, J. Chem. Phys. 129 (2008) 014507.

[46] J.D. Dickson, T.W. Ash, G.B. Williams, A.L. Sukstanskii, R.E. Ansorge, D.A. Yablonskiy, Quantitative phenomenological model of the BOLD contrast mechanism, J. Magn. Reson. 212 (2011) 17–25.

[47] W.R. Bauer, W. Nadler, M. Bock, L.R. Schad, C. Wacker, A. Hartlep, G. Ertl, The relationship between the BOLD-induced T2 and T2*: a theoretical approach for the vasculature of myocardium, Magn. Reson. Med. 42 (1999) 1004–1010.

[48] W.R. Bauer, W. Nadler, M. Bock, L.R. Schad, C. Wacker, A. Hartlep, G. Ertl, Theory of the BOLD effect in the capillary region: an analytical approach for the determination of T2 in the capillary network of myocardium, Magn. Reson. Med. 41 (1999) 51–62.

[49] L.R. Buschle, C.H. Ziener, K. Zhang, V.J.F. Sturm, T. Kampf, A. Hahn, G. Solecki, F. Winkler, M. Bendszus, S. Heiland, H.P. Schlemmer, F.T. Kurz, Vessel radius mapping in an extended model of transverse relaxation, Magn. Reson. Mater. Phys. 31 (2018) 531–551.

[50] T.H. Jochimsen, H.E. Moller, Increasing specificity in functional magnetic resonance imaging by estimation of vessel size based on changes in blood oxygenation, Neuroimage 40 (1) (2008) 228–236.

[51] G.N. Watson, A Treatise on the Theory of Bessel Functions, Cambridge University Press, 1995.

[52] A. Krogh, The supply of oxygen to the tissues and the regulation of the capillary circulation, J. Physiol. 52 (1919) 457–474.

[53] E.C. Titchmarsh, Weber's integral theorem, Proc. Lond. Math. Soc. 2 (1) (1924) 15–28.

[54] C.H. Ziener, T. Kampf, G. Melkus, P.M. Jakob, H.P. Schlemmer, W.R. Bauer, Signal evolution in the local magnetic field of a capillary – analogy to the damped driven harmonic oscillator, Magn. Reson. Imag. 30 (2012) 540–553.